Mon. Not. R. Astron. Soc. **000**, 1–12 (2007) Printed 4 March 2008 (MN LaTeX style file v2.2)

Probing dark energy with steerable wavelets through correlation of WMAP and NVSS local morphological measures

J. D. McEwen[1]*, Y. Wiaux[2], M. P. Hobson[1], P. Vandergheynst[2], A. N. Lasenby[1]
[1]*Astrophysics Group, Cavendish Laboratory, J. J. Thomson Avenue, Cambridge CB3 0HE, UK*
[2]*Signal Processing Institute, Ecole Polytechnique Fédérale de Lausanne (EPFL), CH-1015 Lausanne, Switzerland*

Accepted 27 November 2007. Received 27 November 2007; in original form 12 April 2007

ABSTRACT
Using local morphological measures on the sphere defined through a steerable wavelet analysis, we examine the three-year WMAP and the NVSS data for correlation induced by the integrated Sachs-Wolfe (ISW) effect. The steerable wavelet constructed from the second derivative of a Gaussian allows one to define three local morphological measures, namely the signed-intensity, orientation and elongation of local features. Detections of correlation between the WMAP and NVSS data are made with each of these morphological measures. The most significant detection is obtained in the correlation of the signed-intensity of local features at a significance of 99.9%. By inspecting signed-intensity sky maps, it is possible for the first time to see the correlation between the WMAP and NVSS data by eye. Foreground contamination and instrumental systematics in the WMAP data are ruled out as the source of all significant detections of correlation. Our results provide new insight on the ISW effect by probing the morphological nature of the correlation induced between the cosmic microwave background and large scale structure of the Universe. Given the current constraints on the flatness of the Universe, our detection of the ISW effect again provides direct and independent evidence for dark energy. Moreover, this new morphological analysis may be used in future to help us to better understand the nature of dark energy.

Key words: cosmic microwave background – cosmology: observations – methods: data analysis – methods: numerical.

1 INTRODUCTION

A cosmological concordance model has emerged recently, explaining many observations of our Universe to very good approximation. In this model our Universe is dominated by an exotic dark energy component that may be described by a cosmological fluid with negative pressure, interacting only gravitationally to counteract the attractive gravitational nature of matter. Dark energy may be strongly inferred from observations of the cosmic microwave background (CMB), such as the Wilkinson Microwave Anisotropy Probe (WMAP) data (Bennett et al. 2003b; Hinshaw et al. 2007), together with either observations of Type Ia Supernovae (Riess et al. 1998; Perlmutter et al. 1999) or of the large scale structure (LSS) of the Universe (*e.g.* Allen et al. 2002). Although dark energy dominates the energy density of our Universe, we know very little about its origin and nature. Indeed, a consistent model to describe dark energy in the framework of particle physics is lacking.

The integrated Sachs-Wolfe (ISW) effect (Sachs & Wolfe 1967) provides an independent physical phenomenon that may be used to detect and probe dark energy. As CMB photons travel towards us from the surface of last scattering they pass through gravitational potential wells due to the LSS. If the gravitational potential evolves during the photon propagation, then the photon undergoes an energy shift. The ISW effect is the integrated sum of this energy shift along the photon path. In a matter-dominated Einstein-de Sitter universe the gravitational potential remains constant with respect to conformal time, thus there is no ISW effect. However, if the universe deviates from matter domination due to curvature or dark energy then an ISW effect is induced. Strong constraints have been placed on the flatness of the Universe by WMAP (Spergel et al. 2007), hence a detection of the ISW effect may be inferred as direct and independent confirmation of dark energy.

It is difficult to isolate the ISW contribution to CMB anisotropies directly, therefore Crittenden & Turok (1996) suggested that the ISW effect be detected by cross-correlating CMB anisotropies with tracers of the local matter distribution, such as the nearby galaxy density distribution. A positive large-scale correlation will be induced by the ISW effect as a consequence of decaying gravitational potentials due to dark energy. First attempts to detect the ISW effect using Cosmic Background Explorer-Differential Microwave Radiometer (COBE-DMR) data

* E-mail: mcewen@mrao.cam.ac.uk

failed, concluding that greater sensitivity and resolution than that provided by COBE were required (Boughn & Crittenden 2002). Fortunately, the WMAP mission soon provided suitable CMB data. Correlations indicative of the ISW effect have now been detected between both the first- and three-year WMAP data and a large number of tracers of the LSS. Detections have been made using NRAO VLA Sky Survey (NVSS; Condon et al. 1998) data (Boughn & Crittenden 2004; Nolta et al. 2004; Vielva et al. 2006; McEwen et al. 2007b; Pietrobon et al. 2006), hard X-ray data provided by the High Energy Astronomy Observatory-1 satellite (HEAO-1; Boldt 1987) (Boughn & Crittenden 2005, 2004), APM galaxy survey (Maddox et al. 1990) data (Fosalba & Gaztañaga 2004), Sloan Digital Sky Survey (SDSS; York D. G. *et al.* (SDSS collaboration) 2000) data (Scranton et al. 2003; Fosalba et al. 2003; Padmanabhan et al. 2005; Cabré et al. 2006; Giannantonio et al. 2006), the Two Micron All Sky Survey Extended Source Catalogue (2MASS XSC; Jarrett et al. 2000) (Afshordi et al. 2004; Rassat et al. 2006) and combinations of the aforementioned data sets (Gaztañaga et al. 2006). Furthermore, a number of other works have focused on theoretical detectability, future experiments and/or error analyses related to ISW detections (Afshordi 2004; Hu & Scranton 2004; Pogosian 2005, 2006; Pogosian et al. 2005; Corasaniti et al. 2005; LoVerde et al. 2007; Cabré et al. 2007).

Many different analysis techniques have been employed in these previous works to detect correlations between the data sets, each of which have their own merits and limitations. In this work we focus on wavelet-based techniques. Wavelets provide an ideal analysis tool to search for the ISW effect. This is due to the localised nature of the effect, in both scale and position on the sky, and the simultaneous scale and position localisation afforded by a wavelet analysis. Since the ISW effect is cosmic variance limited, it is desirable to examine as great a sky coverage as possible. In this near full-sky setting the geometry of the sphere should be taken into account, thus wavelet analyses on the sphere are required. The first analysis using wavelets on the sphere to search for correlations between the CMB and LSS was performed by Vielva et al. (2006) using the axisymmetric spherical Mexican hat wavelet. McEwen et al. (2007b) extended this analysis to directional wavelets, as correlated features induced by the ISW effect may not necessarily be rotationally invariant. Indeed, it is known that statistically isotropic Gaussian random fields are characterised by local features that are not rotationally invariant (Barreiro et al. 1997, 2001). Recently, Pietrobon et al. (2006) applied a new wavelet construction on the sphere called needlets to search for correlations. All of these works examined the WMAP and NVSS data (due to the large sky coverage of the NVSS data) and made significant detections of the ISW effect. Moreover, in each analysis the detection of the ISW effect was used to constrain dark energy parameters.

In this paper we present a new search for correlation between the three-year WMAP and the NVSS data using wavelets on the sphere. However, the approach taken here differs fundamentally to previous wavelet analyses. We use steerable wavelets on the sphere to extract, from each of the two data sets, measures of the morphology of local features, such as their signed-intensity, their orientation, or their elongation. We then correlate the WMAP and NVSS data through these quantities. This represents the first direct analysis of local morphological measures on the sphere resulting from the steerability of wavelets. A positive detection of correlation using any of these morphological probes would give a direct indication of the ISW effect, provided it were not due to unremoved foregrounds or measurement systematics, which could again be inferred as direct and independent evidence for dark energy. Moreover, such a detection would give an indication of the morphological nature of the correlation. This further insight might help to better understand the nature of dark energy. However, the derivation of the theoretical correlation of the newly defined morphological measures as a function of the dark energy content of the Universe is not easily tractable. Consequently, corresponding constraints on dark energy parameters are left to a future work.

The remainder of this paper is organised as follows. In section 2 we present the physical and signal processing background behind the analyses performed. The ISW effect is described and the use of local morphological measures defined through a steerable wavelet analysis is presented as a probe to search for the ISW effect. In section 3 the data and analysis procedures employed are described in detail. Two distinct analysis techniques are proposed to compute correlations from morphological measures: a *local morphological analysis* and a *matched intensity analysis*. The results of these analyses are presented in section 4 and section 5 respectively. Concluding remarks are made in section 6.

2 ISW EFFECT AND STEERABLE WAVELETS

The existence of an ISW effect induces a cross-correlation between the CMB and NVSS signals on the celestial sphere. From the spectral point of view, the corresponding two-point cross-correlation function may be expressed in terms of the cross-correlation angular power spectrum. In this paper, we go beyond this spectral analysis thanks to a decomposition of the CMB and NVSS signals with steerable wavelets on the sphere. The wavelet analysis enables one to probe local features at each analysis scale. In this section we first review the ISW effect and the correlation between the CMB and NVSS data that it induces. Secondly, we discuss wavelets on the sphere and describe how the steerability of wavelets is used to define local morphological measures on the sphere.

2.1 ISW effect

The secondary temperature anisotropy induced in the CMB by the ISW effect is related to the evolution of the gravitational potential. Any recent acceleration of the scale factor of the Universe due to dark energy will cause local gravitational potentials to decay. CMB photons passing through over dense regions of decaying potential suffer blue shifts, resulting in a positive correlation between the induced anisotropy and the local matter distribution. It can be shown that the relative temperature fluctuation induced in the CMB is given by

$$\Delta^{\mathrm{T}}(\omega) = \frac{\Delta T(\omega)}{T_0} = -2 \int \mathrm{d}\eta \, \dot{\Phi}(\eta, \omega) \tag{1}$$

(Sachs & Wolfe 1967; Nolta et al. 2004), where ΔT is the induced temperature perturbation, T_0 is the mean temperature of the CMB, η is conformal time, Φ is the gravitational potential and the dot represents a derivative with respect to conformal time. A point ω on the sky is represented in spherical coordinates as $\omega = (\theta, \varphi)$, with co-latitude θ and longitude φ. The integral is computed over the photon path from emission to observation, *i.e.* from today back to the last scattering surface. In a matter-dominated Einstein-de Sitter universe (with zero cosmological constant) the potential evolves as $\Phi \sim \delta/R$, where δ is the matter perturbation and R is the scale factor of the universe. In this setting the matter perturbation evolves with the scale factor, $\delta \propto R$. Consequently, $\dot{\Phi} = 0$ and there is no ISW effect, as discussed previously.

We use the NVSS galaxy count distribution projected onto the sky as a tracer of the local matter distribution. It is assumed that the two corresponding relative fluctuations, respectively $\delta^{\mathrm{N}}(z,\omega)$ and $\delta(z,\omega)$, are related by the linear bias factor $b(z)$: $\delta^{\mathrm{N}}(z,\omega) = b(z)\,\delta(z,\omega)$, where z is redshift. Hereafter we take the bias to be redshift independent since the redshift epoch over which the ISW effect is produced is small. The galaxy source count fluctuation observed on the sky is therefore given by

$$\Delta^{\mathrm{N}}(\omega) = b \int \mathrm{d}z\, \frac{\mathrm{d}N}{\mathrm{d}z}\, \delta(z,\omega)\,, \tag{2}$$

where $\mathrm{d}N/\,\mathrm{d}z$ is the mean number of sources per steradian at redshift z and the integral is performed from today to the epoch of recombination, *i.e.* last scattering.

We are now in a position to consider the correlation between the galaxy count and CMB temperature fluctuations. We consider the cross-power spectrum C_ℓ^{NT} defined by the ensemble average of the product of the spherical harmonic coefficients of the two signals observed on the sky:

$$\langle \Delta^{\mathrm{N}}_{\ell n}\, \Delta^{\mathrm{T}\,*}_{\ell' n'} \rangle = \delta_{\ell\ell'}\delta_{nn'}\, C_\ell^{\mathrm{NT}}\,, \tag{3}$$

where $\Delta_{\ell n} = \langle Y_{\ell n} | \Delta \rangle$ are the spherical harmonic coefficients of $\Delta(\omega)$, $\langle\cdot|\cdot\rangle$ denotes the inner product on the sphere, $Y_{\ell n}$ are the spherical harmonic functions for multipole $\ell \in \mathbb{N}$, $n \in \mathbb{Z}$, $|n| \leqslant \ell$ and δ_{ij} is the Kronecker delta symbol. In writing the cross-correlation in this manner we implicitly assume that the galaxy density and CMB random fields on the sphere are homogeneous and isotropic, which holds under the basic assumption of the cosmological principle. Representing the gravitational potential and the matter density perturbation in Fourier space and substituting (1) and (2) into (3), it is possible to show (*e.g.* Nolta et al. 2004) that

$$C_\ell^{\mathrm{NT}} = 12\pi\, \Omega_{\mathrm{m}}\, {H_0}^2 \int \frac{\mathrm{d}k}{k^3}\, \Delta^2_\delta(k)\, F^{\mathrm{N}}_\ell(k)\, F^{\mathrm{T}}_\ell(k)\,, \tag{4}$$

where Ω_{m} is the matter density, H_0 is the Hubble parameter, $\Delta^2_\delta(k) = k^3 P_\delta(k)/2\pi^2$ is the logarithmic matter power spectrum, $P_\delta(k) = \langle|\delta(k)|^2\rangle$ is the matter power spectrum and the filter functions for the galaxy density and CMB are given by

$$F^{\mathrm{N}}_\ell(k) = b \int \mathrm{d}z\, \frac{\mathrm{d}N}{\mathrm{d}z}\, D(z)\, j_\ell[k\eta(z)] \tag{5}$$

and

$$F^{\mathrm{T}}_\ell(k) = \int \mathrm{d}z\, \frac{\mathrm{d}g}{\mathrm{d}z}\, j_\ell[k\eta(z)] \tag{6}$$

respectively. The integration required to compute $F^{\mathrm{T}}_\ell(k)$ is performed over z from zero to the epoch of recombination, whereas, in practice, the integration range for $F^{\mathrm{N}}_\ell(k)$ is defined by the source redshift distribution $\mathrm{d}N/\,\mathrm{d}z$. $D(z)$ is the linear growth factor for the matter distribution: $\delta(z,k) = D(z)\delta(k)$, with $\delta(k) = \delta(0,k)$. The function $g(z) \equiv (1+z)D(z)$ is the linear growth suppression factor and $j_\ell(\cdot)$ is the spherical Bessel function. We have represented in harmonic space the expected correlation between the galaxy source count fluctuations and the CMB temperature fluctuations induced by the ISW effect. We next turn our attention to steerable wavelets on the sphere as a potential tool for detecting this correlation.

2.2 Wavelets on the sphere

The WMAP and NVSS data may be understood as the sampling of continuous signals on the sphere, which can be analysed in the framework of a continuous wavelet formalism. The analysis of a signal on the sphere with a wavelet, which is a local analysis function, yields a set of wavelet coefficients. These coefficients result from the scalar products between the signal and the wavelet dilated at any scale, rotated around itself by any angle, and translated at any point on the sphere. The so-called steerable wavelets allow, from these wavelet coefficients, the definition of local morphological measures of the signal. In particular, the second Gaussian derivative wavelet used in the present analysis gives access to the measures of orientation, signed-intensity, and elongation of the signal's local features. The remainder of this section is devoted to the explicit definition of these local morphological measures. The reader not directly interested in these formal and technical details may proceed directly to section 3.

The continuous wavelet formalism on the sphere originally proposed by Antoine & Vandergheynst (1998) was recently further developed in a practical approach by Wiaux et al. (2005). It defines the wavelet decomposition of a signal on the sphere in the following way. We consider an orthonormal Cartesian coordinate system $(o, o\hat{x}, o\hat{y}, o\hat{z})$ centred on the (unit) sphere, with the direction $o\hat{z}$ defining the North Pole. To relate this coordinate system to the spherical coordinates $\omega = (\theta, \varphi)$ defined previously, we let the polar angle, or co-latitude, $\theta \in [0, \pi]$ represent the angle between the vector identifying ω and the axis $o\hat{z}$, and the azimuthal angle, or longitude, $\varphi \in [0, 2\pi)$ represent the angle between the orthogonal projection of this vector in the plane $(o, o\hat{x}, o\hat{y})$ and the axis $o\hat{x}$.

The signal to be analysed is represented by a square-integrable function $F(\omega)$ on the sphere, *i.e.* $F(\omega) \in L^2(S^2,\, \mathrm{d}\Omega)$, for the invariant measure $\mathrm{d}\Omega = \mathrm{d}(\cos\theta)\,\mathrm{d}\varphi$. A square-integrable analysis function $\Psi(\omega)$ is defined, the so-called mother wavelet, initially centred at the North Pole. This wavelet may be dilated at any scale $a > 0$. The dilation of a wavelet on the sphere in this formalism may be uniquely related to the usual dilation in the tangent plane at the north pole (as discussed in more detail below). The corresponding Ψ_a can cover arbitrarily small or large regions of the sphere, respectively corresponding to high or low frequencies. Through the appropriate three-dimensional rotation, the wavelet may also be rotated on itself by any angle $\chi \in [0, 2\pi)$ and translated to any point $\omega_0 = (\theta_0, \varphi_0)$ on the sphere. The final dilated, rotated and translated wavelet is denoted $\Psi_{\omega_0,\chi,a}$. At each scale, the wavelet coefficients of the signal are defined by the directional correlation with Ψ_a, *i.e.* by the simple scalar product

$$W^F_\Psi(\omega_0, \chi, a) = \langle \Psi_{\omega_0,\chi,a} | F \rangle \equiv \int_{S^2} \mathrm{d}\Omega\, \Psi^*_{\omega_0,\chi,a}(\omega)\, F(\omega)\,, \tag{7}$$

where the superscript * denotes complex conjugation. These wavelet coefficients hence characterise the signal locally around each point ω_0, at scale a and orientation χ. The choice of possible mother wavelets is submitted to a condition ensuring that the original signal can be reconstructed exactly from its wavelet coefficients. In practice, this wavelet admissibility condition on the sphere is not easy to check for a given candidate function. It is therefore difficult to build wavelets directly on the sphere.

A correspondence principle has been established (Wiaux et al. 2005), which states that the inverse stereographic projection of a wavelet on the plane provides a wavelet on the sphere. The stereographic projection of a point $\omega = (\theta, \varphi)$ on the sphere gives by definition a point $\vec{x} = (r, \varphi)$ on its tangent plane at the North pole, which is co-linear with ω and the South Pole. It relates the radial variables on the two manifolds through the bijection $r(\theta) = 2\tan(\theta/2)$, and simply identifies the angular variables φ (see Fig. 1). If the corresponding unitary operator on functions is denoted Π, the correspon-

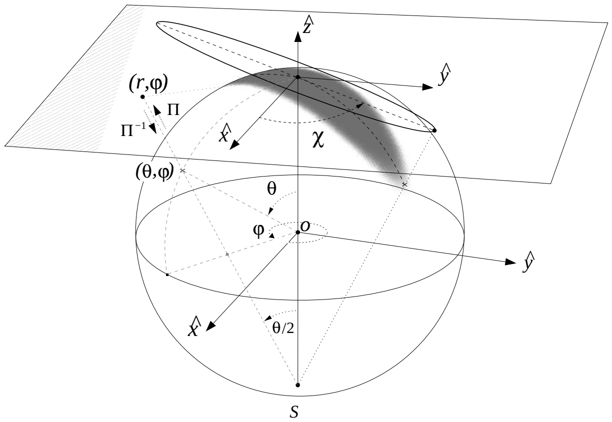

Figure 1. Wavelets on the sphere can be defined through simple inverse stereographic projection Π^{-1} of wavelets on the tangent plane at the North pole. The corresponding functions are illustrated here by the shadow on the sphere and the localised region on the plane. (Illustration reproduced from Wiaux et al. 2005.)

dence principle states that, if $\psi(\vec{x})$ is a wavelet on the plane, then $\Psi(\omega) = [\Pi^{-1}\psi](\omega)$ is a wavelet on the sphere.

The dilation of a wavelet on the sphere actually corresponds to the conjugate, through the stereographic projection, of the usual dilation in the tangent plane at the north pole. This conjugation relation also trivially holds for the rotation of wavelets by χ, which only affects the longitude, while the stereographic projection leaves it invariant. In other words, the dilation and rotation of the wavelet on itself may be performed through the natural dilation and rotation on the plane before projection:

$$\Psi_{\chi,a}(\omega) = [\Pi^{-1}\psi_{\chi,a}](\omega)\,. \tag{8}$$

Only the translation by ω_0 must be performed explicitly on the sphere through the appropriate rotation in three dimensions. As wavelets on the plane are well-known and may be easily built as simple zero-mean filters, the correspondence principle enables one to define a large variety of wavelets on the sphere by simple projection. This principle also allows one to transfer wavelet properties from the plane onto the sphere, such as the notion of steerability discussed in the next section.

The wavelet analysis on the sphere described above is computationally demanding. The directional correlation described by (7) requires the evaluation of a two-dimensional integral over a three-dimensional domain. Direct computation of this integral by simple quadrature is not computationally feasible for practical CMB data, such as the currently available 3 megapixel WMAP maps and the forthcoming 50 megapixel Planck (Planck collaboration 2005) maps. Fast algorithms to compute the wavelet decomposition of signals on the sphere have been developed and implemented by Wiaux et al. (2006) and McEwen et al. (2007a) (for a review see Wiaux et al. invited contribution, 2007). In this work we utilise the implementation described by McEwen et al. (2007a).

2.3 Steerability and morphological measures

Firstly, we review the notion of steerable wavelets on the sphere. Just as on the plane, a function on the sphere is said to be axisymmetric if it is invariant under rotations around itself. Any non-axisymmetric function is called directional. The directionality of a wavelet is essential in allowing one to probe the direction of local features in a signal. A wavelet is said to be steerable if its rotation around itself by any angle χ may be written as a simple linear combination of non-rotated basis filters. On the sphere, for M basis filters Ψ_m, a steerable wavelet may be written, by definition, as

$$\Psi_{\chi}(\omega) = \sum_{m=1}^{M} k_m(\chi)\Psi_m(\omega) \tag{9}$$

(Wiaux et al. 2005). The weights $k_m(\chi)$, with $1 \leqslant m \leqslant M$, are called interpolation functions. In particular cases, the basis filters may be specific rotations by angles χ_m of the original wavelet: $\Psi_m = \Psi_{\chi_m}$. Steerable wavelets have a non-zero angular width in the azimuthal angle φ. This property makes them sensitive to a range of directions and enables them to satisfy their relation of definition. In spherical harmonic space, this non-zero angular width corresponds to an azimuthal angular band limit N in the integer index n associated with the azimuthal variable φ: $\Psi_{\ell n} = 0$ for $|n| \geqslant N$. Typically, the number M of interpolating functions is of the same order as the azimuthal band limit N. Notice that the steerability is a property related to the azimuthal variable φ only. Again as the stereographic projection only affects the radial variables, steerable wavelets on the sphere can easily be built as simple inverse stereographic projection of steerable wavelets on the plane.

The derivatives of order $N_{\rm d}$ in direction $\hat{x}$ of radial functions $\phi(r)$ on the plane are steerable wavelets. The corresponding steerable wavelets on the sphere produced by inverse stereographic projection may be rotated in terms of $M = N_{\rm d} + 1$ basis filters, and are band-limited in φ at $N = N_{\rm d} + 1$. The second derivative $\Psi^{\partial^2_{\hat{x}}}$ of any radial function has a band limit $N = 3$, and contains the frequencies $n = \{0, \pm 2\}$ only. $\Psi^{\partial^2_{\hat{x}}}$ may be rotated in terms of three basis filters: the second derivatives in directions $\hat{x}$ and $\hat{y}$, $\Psi_1 = \Psi^{\partial^2_{\hat{x}}}$ and $\Psi_2 = \Psi^{\partial^2_{\hat{y}}}$, and the cross derivative $\Psi_3 = \Psi^{\partial_{\hat{x}}\partial_{\hat{y}}}$, with the corresponding weights $k_1(\chi) = \cos^2\chi$, $k_2(\chi) = \sin^2\chi$, and $k_3(\chi) = \sin 2\chi$. Fig. 2 illustrates the explicit example of the second derivative of a Gaussian, which is the wavelet employed in the subsequent analysis. In this case, the original radial function on the plane is given as $\phi^{(Gauss)}(r) = -\sqrt{4/3\pi}e^{-r^2/2}$, with proper normalisation ensuring that the mother wavelet $\Psi^{\partial^2_{\hat{x}}(Gauss)}$ on the sphere is normalised to unity. The explicit basis filters obtained by differentiation are analytically defined by Wiaux et al. (2006). Recall that the natural dilation on the tangent plane at the North Pole sends the radial variable $r(\theta)$ onto $r(\theta)/a$. The value of the scale a therefore identifies with the dispersion of the Gaussian. Consequently, we define the angular size of our second Gaussian derivative wavelet on the sphere as twice the *half-width* of the wavelet, where the half-width is defined by $\theta_{\rm hw} = 2\arctan(a/2)$, which is closely approximated by a at small scales.

We use wavelet steerability to define local morphological measures of real signals F on the sphere. Local geometrical quantities have previously been defined in real space, and have been used to analyse CMB data and test cosmological models (Barreiro et al. 1997, 2001; Monteserín et al. 2005; Gurzadyan et al. 2005). Our approach in wavelet space is completely novel. By linearity of the wavelet decomposition, the steerability relation also holds on the wavelet coefficients of a signal F,

$$W^F_{\Psi}(\omega_0, \chi, a) = \sum_{m=1}^{M} k_m(\chi)\, W^F_{\Psi_m}(\omega_0, a)\ , \tag{10}$$

where the coefficients $W^F_{\Psi_m}(\omega_0, a)$ result from the correlation of F with the non-rotated ($\chi = 0$) filter Ψ_m at scale a. Technically these M coefficients thus gather all the local information retained by the steerable wavelet analysis at the point ω_0 and at the scale a. One

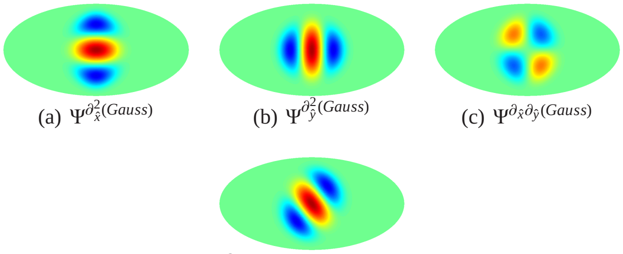

(a) $\Psi^{\partial^2_{\hat{x}}(Gauss)}$ (b) $\Psi^{\partial^2_{\hat{y}}(Gauss)}$ (c) $\Psi^{\partial_{\hat{x}}\partial_{\hat{y}}(Gauss)}$

(d) $\Psi^{\partial^2_{\hat{x}}(Gauss)}$ rotated by $\chi = \pi/4$

Figure 2. Mollweide projection of second Gaussian derivative wavelet on the sphere for wavelet half-width $\theta_{\rm hw} \simeq 0.4$ rad. The rotated wavelet illustrated in panel (d) can be constructed from a sum of weighted versions of the basis wavelets illustrated in panels (a) through (c).

may be willing to reorganise this information in terms of M quantities with an explicit local morphological meaning. For $M = 1$, the steerable wavelet is actually axisymmetric, and only a measure of signed-intensity $I^F(\omega_0, a)$ of local features in the signal is accessible (given by the wavelet coefficient $W^F_\Psi(\omega_0, a)$ directly). For $M \geqslant 2$, the steerable wavelet is directional and the orientation, or direction, $D^F(\omega_0, a)$ of local features may be accessed through the value which maximises the wavelet coefficient. The signed-intensity $I^F(\omega_0, a)$ of the local feature is given by that coefficient of maximum absolute value. Additional local morphological measures may be defined for $M \geqslant 3$, notably a measure of the elongation of local features, probing their non-axisymmetry, in addition to their signed-intensity and orientation. As the wavelet coefficient in each orientation naturally probes the extension of the local feature in the corresponding direction, this elongation $E^F(\omega_0, a)$ can simply be measured from the absolute value of the ratio of the wavelet coefficient of maximum absolute value, to the wavelet coefficient in the perpendicular direction. The higher the number M of basis filters, the wider the accessible range of local morphological measures.

Any second derivative of a radial function, such as the second Gaussian derivative, is defined from $M = 3$ basis filters. The signed-intensity, orientation, and elongation are therefore accessible in this case. Because the mother wavelet $\Psi^{\partial^2_{\hat{x}}}$ oscillates in the tangent direction $\hat{x}$, it actually detects features oriented along the tangent direction $\hat{y}$. The orientation of local features is therefore given as

$$\frac{\pi}{2} \leqslant \quad D^F(\omega_0, a) \equiv \chi_0 + \frac{\pi}{2} \quad < \frac{3\pi}{2} \,, \tag{11}$$

where the orientation $\chi_0 \equiv \chi_0(\omega_0, a)$ that maximises the wavelet coefficient can be analytically defined from (10). Notice that the second derivative of a radial function is invariant under a rotation by π around itself. Consequently, the local orientations define headless vectors in the tangent plane at ω_0. By convention the corresponding vectors are chosen to point towards the Northern hemisphere only, and the local orientations are therefore in the range $[\pi/2, 3\pi/2)$. For a second derivative of a radial function, as for any real steerable wavelet, the signed-intensity of local features is given by the wavelet coefficient in the direction χ_0:

$$I^F(\omega_0, a) \equiv W^F_{\Psi^{\partial^2_{\hat{x}}}}(\omega_0, \chi_0, a) \,. \tag{12}$$

The elongation of local features analysed by the second derivative of a radial function is explicitly defined by

$$0 \leqslant \quad E^F(\omega_0, a) \equiv 1 - \left| \frac{W^F_{\Psi^{\partial^2_{\hat{x}}}}\left(\omega_0, \chi_0 + \frac{\pi}{2}, a\right)}{W^F_{\Psi^{\partial^2_{\hat{x}}}}(\omega_0, \chi_0, a)} \right| \quad \leqslant 1 \,. \tag{13}$$

Numerical tests performed on elliptical Gaussian-profile features show that this elongation measure for the second Gaussian derivative increases monotonously in the range $[0, 1]$ with the intrinsic eccentricity $e \in [0, 1]$ of the features. While it is possible to define alternative elongation measures, these numerical tests indicate that the chosen definition is not an arbitrary measure of the non-axisymmetry of local features, but represents a rough estimate of the eccentricity of a Gaussian-profile local feature.

3 ANALYSIS PROCEDURES

The data and analysis procedures that we use in an attempt to detect the ISW effect are described in detail in this section. We propose two distinct analysis techniques based on the correlation of the local morphological measures on the sphere defined in section 2.3. After describing the data, we discuss the generic procedure to search for any correlation between the NVSS and WMAP data. We then describe in detail the two approaches proposed, motivating the analyses and highlighting the differences between them.

3.1 Data and simulations

In this work we examine the three-year release of the WMAP data and the NVSS data for correlations induced by the ISW effect. Here we briefly describe the data, preprocessing of the data and the simulations performed to quantify any correlations detected in the data.

We examine the co-added three-year WMAP sky map. This map is constructed from a noise weighted sum of the maps observed by the Q-, V- and W- channels of WMAP, in order to enhance the signal-to-noise ratio of the resultant map. The co-added map was first introduced by the WMAP team in their non-Gaussianity analysis (Komatsu et al. 2003) and has since been used in numerous analyses. We use the template based foreground cleaned WMAP band maps (Bennett et al. 2003a) to construct the co-added map. The conservative Kp0 mask provided by the WMAP team is used to remove remaining Galactic emission and bright point sources. Since the ISW effect is expected to induce correlations on scales $> 2^\circ$ (Afshordi 2004), we downsample the co-added map to a pixel size of $\sim 55'$ (a `HEALPix`[1] (Górski et al. 2005) resolution of $N_{\rm side} = 64$). This reduces the computation requirements of the subsequent analysis considerably, while ensuring the analysis remains sensitive to ISW induced correlations.

The large sky coverage and source distribution of the NVSS data make it an ideal probe of the local matter distribution to use when searching for the ISW effect. Sources in the catalogue are thought to be distributed in the range $0 < z < 2$, with a peak distribution at $z \sim 0.8$ (Boughn & Crittenden 2002). This corresponds closely to redshift regions where the ISW signal that we hope to detect is produced (Afshordi 2004). The NVSS source distribution is projected onto the sky in a `HEALPix` representation at the same resolution as the WMAP co-added map considered (*i.e.* $N_{\rm side} = 64$) and an important systematic in the data is corrected. The correction of this systematic and the resulting preprocessed NVSS data examined here are both identical to that analysed in McEwen et al. (2007b), hence we refer the interested reader to this work for more

[1] `http://healpix.jpl.nasa.gov/`

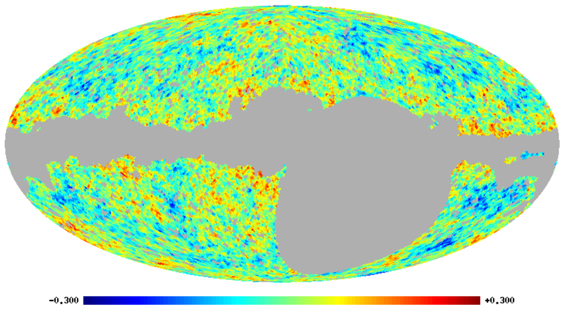

(a) WMAP

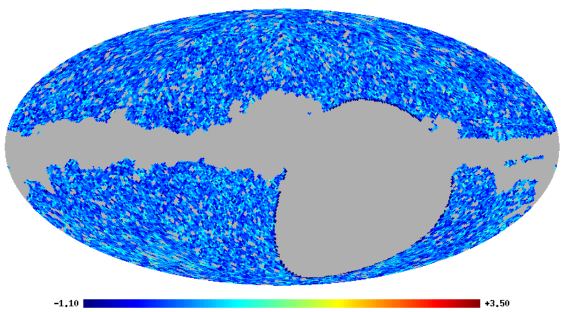

(b) NVSS

Figure 3. WMAP co-added three-year and NVSS maps (Mollweide projection) after application of the joint mask. The maps are downsampled to a pixel size of ~55′. The WMAP temperature data are reported in mK, while the NVSS data are reported in number-of-counts per pixel.

details of the data preprocessing. Not all of the sky is sufficiently observed in the NVSS catalogue. We construct a joint mask to exclude from our subsequent analysis those regions of the sky not observed in the catalogue, in addition to the regions excluded by the WMAP Kp0 mask. The WMAP and NVSS data analysed subsequently, with the joint mask applied, are illustrated in Fig. 3.

In order to constrain the statistical significance of any detection of correlation between the WMAP and NVSS data we perform Monte Carlo simulations. 1000 simulations of the WMAP co-added map are constructed, modelling carefully the beam and anisotropic noise properties of each of the WMAP channels and mimicking the co-added map construction procedure (including the downsampling stage). The analyses subsequently performed on the data are repeated on the simulations and compared.

3.2 Generic procedure

Two different analysis procedures are applied to test the data for correlation. The first procedure correlates the local morphological measures of signed-intensity, orientation and elongation, extracted independently from the two data sets. This procedure does not rely on any assumption about the correlation in the data. The second procedure correlates local features in the WMAP data that are matched in orientation to local features extracted from the NVSS data. This approach explicitly assumes that local features of the LSS are somehow included in the CMB. In the absence of any ISW effect one would not expect to detect any significant correlation in either of these analyses. The analysis procedures are described in more detail in the following subsections. Firstly, we describe the generic part of the procedure common to both techniques.

We consider only those scales where the ISW effect is expected to be significant (Afshordi 2004), *i.e.* scales approximately corresponding to wavelet half-widths $\theta_{\rm hw}$ of $\{100', 150', 200', 250', 300', 400', 500', 600'\}$. The local morphological measures defined in section 2.3 are computed for the WMAP and NVSS data and are used to compute various correlation statistics (see the following subsections for more detail). Identical statistics are computed for the Monte Carlo simulations in order to measure the statistical significance of any correlation detected in the data. A statistically significant correlation in the data apparent from any of these statistics is an indication of the ISW effect, provided it is not due to foreground contributions or systematics.

The procedure described previously would be sufficient for data with full-sky coverage. Unfortunately this is not the case and the application of the joint mask must be taken into account. The application of the mask distorts those morphological quantities constructed from wavelets with support that overlaps the mask exclusion regions. The associated local morphological measures must be excluded from the analysis. An extended mask is computed for each scale to remove all contaminated values. The extended masks are constructed by extending the central masked region by the wavelet half-width, whilst maintaining the size of point source regions in the mask. We use identical masks to those applied by McEwen et al. (2007b) and refer the interested reader to this work for more details.

Before proceeding with our morphological analyses it is important to check that the WMAP and NVSS data do not contain predominantly axisymmetric features, corresponding to local elongation trivially equal to zero and for which no local orientation might be defined. To do this we examine the distribution of our morphological measure of elongation defined in section 2.3. In Fig. 4 we plot the histograms of the elongation measures computed from the data (outside of the extended exclusion masks). These histograms are built from all scales but the distributions obtained for each individual scale also exhibit similar structure. Many elongation values computed from both data sets lie far from zero, thereby justifying the morphological analyses that we propose.

In order to give some intuition on the magnitude of various statistics computed in the remainder of this paper, we also quote the orders of magnitude for the means and standard deviations of the different local morphological measures, as estimated from the two data sets. Firstly, the mean and standard deviation of the elongation in the WMAP data are respectively $\hat{\mu}_E^{\rm T} = 0.61$ and $\hat{\sigma}_E^{\rm T} = 0.27$, when data from all scales are gathered. The corresponding values for the NVSS data are $\hat{\mu}_E^{\rm N} = 0.62$ and $\hat{\sigma}_E^{\rm N} = 0.26$. Secondly, recall that the galaxy density and CMB random fields on the sphere are assumed to be homogeneous and isotropic. The local orientations computed from the data sets should therefore reflect a uniform distribution in the range $[\pi/2, 3\pi/2)$. Consistently, the mean and standard deviation of the orientation in the WMAP data are respectively $\hat{\mu}_D^{\rm T} = 3.10$ and $\hat{\sigma}_D^{\rm T} = 0.93$, again gathering data from all scales. The corresponding values for the NVSS data are $\hat{\mu}_D^{\rm N} = 3.10$ and $\hat{\sigma}_D^{\rm N} = 0.90$. Finally, notice that the local signed-intensity of a signal is expressed, *a priori* on the whole real line, in the same units as the signal itself. The signed-intensity of the WMAP temperature fluctuation data is given in mK, while the signed-intensity of the NVSS galaxy source count fluctuation data is given in number-of-counts per pixel (see Fig. 3). The mean and standard deviation of the signed-intensity in the WMAP data are respectively $\hat{\mu}_I^{\rm T} = -2\times10^{-4}$ and $\hat{\sigma}_I^{\rm T} = 6\times10^{-3}$, still accounting for data from all scales. The corresponding values for the NVSS data are $\hat{\mu}_I^{\rm N} = 0.001$ and $\hat{\sigma}_I^{\rm N} = 0.01$.

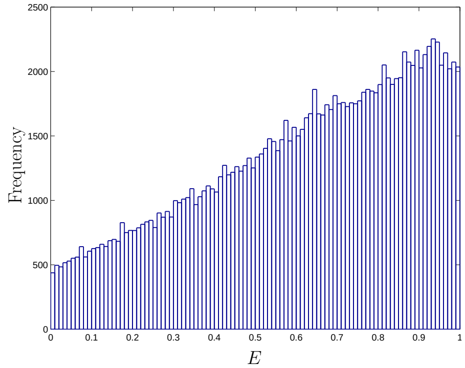

(a) WMAP

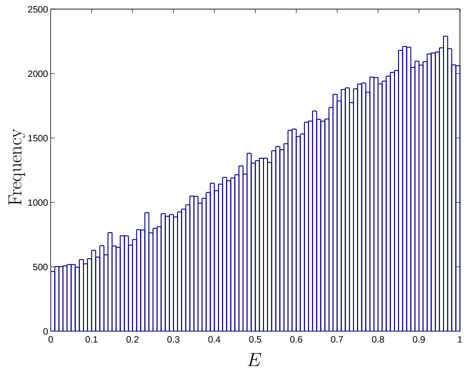

(b) NVSS

Figure 4. Histograms of the elongation values computed from the WMAP and NVSS data for all scales. Many elongation values lie far from zero, thereby justifying the morphological analyses that we propose.

3.3 Local morphological analysis

In the local morphological analysis that follows we correlate the WMAP and NVSS data through each of the morphological measures provided by the second derivative of a Gaussian wavelet separately, *i.e.* the signed-intensity, orientation and elongation of local features. Local features are extracted independently from the WMAP and NVSS data. We then compute the correlation by

$$X_{S_i}^{\mathrm{NT}}(a) = \frac{1}{N_\mathrm{p}} \sum_{\omega_0} S_i^{\mathrm{N}}(\omega_0, a)\, S_i^{\mathrm{T}}(\omega_0, a) - \left[\frac{1}{N_\mathrm{p}} \sum_{\omega_0} S_i^{\mathrm{N}}(\omega_0, a)\right] \cdot \left[\frac{1}{N_\mathrm{p}} \sum_{\omega_0} S_i^{\mathrm{T}}(\omega_0, a)\right], \qquad (14)$$

where $S_i = \{I, D, E\}$ is the morphological measure examined, with superscript N or T representing respectively the NVSS and WMAP data (note that the morphological measures are computed at N_p discrete points on the sky only). This analysis provides the most general approach to computing correlations and does not make any assumption about possible correlation in the data. In the absence of an ISW effect the WMAP and NVSS data should be independent and none of the correlation estimators defined by (14) should exhibit a significant deviation from zero.

3.4 Matched intensity analysis

In the matched intensity analysis that follows we first compute the orientation and signed-intensity of local features for the NVSS data. Using the local orientations extracted from the NVSS data, we compute the signed-intensity of local features in the WMAP data that are matched in orientation to the local features in NVSS data. For this matched intensity analysis it no longer makes sense to examine the correlation of orientations any further since they are identical in both data sets, nor to examine the elongation measures any further since the elongation does not measure the eccentricity of local features in the WMAP data when the orientation is extracted from the NVSS data. We therefore only correlate, through (14) again, the signed-intensity of features extracted from the data. This analysis is based on the assumption that local features in the NVSS data are somehow included in the WMAP data. This is a conceptually different analysis to the local morphological analysis described in the preceding subsection.

Before proceeding with this analysis it is important to check that it differs in practice to the local morphological analysis. To do this we examine the difference in the orientation of local features, extracted independently in each data set, at each position on the sky. From relation (11) it can be seen that this difference technically lies in the range $[-\pi, \pi)$. It is however defined modulo π, and the range is explicitly restricted to $\Delta D \in [-\pi/2, \pi/2)$. If orientation differences are predominantly zero, then we know *a priori* that the two analysis procedures are essentially the same and would give the same result for the correlation of signed-intensities. In Fig. 5 we plot the histogram of the differences in orientation between the two data sets (outside of the extended exclusion masks), built from all scales (the distributions obtained for each individual scale exhibit similar structure). The orientation differences are broadly distributed about zero, thus the two analysis techniques proposed are indeed different practically, as well as conceptually. Moreover, the relative flatness of the distribution suggests no obvious correlation of orientations between the WMAP and NVSS data. This is examined in detail through the local morphological analysis when applied to orientations.

Notice that the local morphological measure of the orientation defined by (11) depends on the coordinate system considered through the definition of the origin $\chi = 0$ at each point on the sphere. The estimator for the correlation of orientations between the two data sets given by (14) also depends on the coordinate system. This dependence does not affect the statistical significance of any correlation detected, which simply measures a possible anomaly between the data and the simulations. One could substitute the estimator (14) by a measure of flatness for the distribution of the difference in the orientation ΔD between the two data sets. This difference is indeed independent of the coordinate system and has a direct physical meaning. However, this would simply provide an alternative measure of the statistical significance of any correlation detected in the orientation of local features. Either estimator is therefore suitable; for consistence we choose the former case.

4 LOCAL MORPHOLOGICAL CORRELATIONS

In this section we present the results obtained from the local morphological analysis described in section 3.3 to examine the WMAP and NVSS data for possible correlation. Correlations are detected and are examined to determine whether they are due to foreground contamination or instrumental systematics, or whether they are indeed induced by the ISW effect.

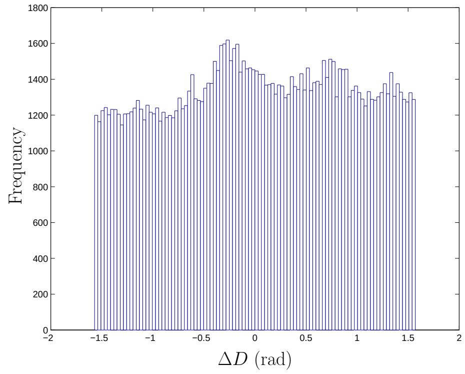

Figure 5. Histogram of the difference in orientation of local features extracted independently in the WMAP and NVSS data for all scales. This difference ΔD is defined modulo π, in the range $[-\pi/2, \pi/2)$. The distribution is not concentrated about zero, indicating that the local morphological and matched intensity analyses are indeed different practically, as well as conceptually.

4.1 Detections

The correlation statistics computed from the WMAP and NVSS data for each morphological measure are displayed in Fig. 6. Significance levels computed from the 1000 Monte Carlo simulations described in section 3.1 are also shown on each plot. A non-zero correlation signal is clearly present in the signed-intensity of local features. A strong detection at 99.3% significance is made in the correlation of signed-intensities for wavelet half-width $\theta_{\rm hw} \simeq 400'$. This correlation deviates from the mean of the Monte Carlo simulations by 2.8 standard deviations. Moderate detections are also made in the correlation of the orientations and elongations of local features for $\theta_{\rm hw} \simeq 400'$ at 93.3% significance and for $\theta_{\rm hw} \simeq 600'$ at 97.2% significance respectively.

The statistical significance of these findings is based on an *a posteriori* selection of the scale corresponding to the most significant correlation. Nevertheless, such statistics have been widely used to quantify detections of the ISW effect, and are satisfactory provided that the *a posteriori* nature of the analysis is acknowledged. However, in this work we also consider a χ^2 analysis to examine the significance of correlation between the data when the correlation statistics for all scales are considered in aggregate. This *a priori* statistic is more conservative in nature; we consider it as a simple alternative detection measure which takes into account the correlation between scales. For the correlation computed for each local morphological measure we compute the χ^2 defined by

$$\chi^2_{S_i} = \boldsymbol{X}^{\rm NT\,\dagger}_{S_i}\, \mathsf{C}^{-1}_{S_i}\, \boldsymbol{X}^{\rm NT}_{S_i}\,, \tag{15}$$

where $\boldsymbol{X}^{\rm NT}_{S_i}$ is a concatenated vector of $X^{\rm NT}_{S_i}(a)$ for all scales, the matrix C_{S_i} is a similarly ordered covariance matrix of the morphological correlation statistics computed from the Monte Carlo simulations and † represents the matrix transpose operation. Comparing the χ^2 values computed from the data to those computed from the Monte Carlo simulations, it is possible to quantify the statistical significance of correlation in the data. Moderate detections are made in the correlation of signed-intensities and orientations of local features at 94.5% and 93.2% significance respectively. The detection in the correlation of elongations drops considerably to 84.5% significance.

The steerable wavelet analysis performed allows one to localise on the sky those regions that contribute most significantly to the correlation detected in the data. This type of localisation was performed by McEwen et al. (2007b). However, it was found in this work that, although the localised regions were a significant source of correlation between the data, they by no means provided the sole contribution of correlation. Similar findings were also obtained by Boughn & Crittenden (2005) using a different analysis technique. These results are consistent with intuitive predictions based on the ISW effect, namely that one would expect to observe correlations weakly distributed over the entire sky, rather than only a few highly correlated localised regions. For these reasons we do not repeat the localisation performed by McEwen et al. (2007b) for the current analysis (especially since we shown in section 4.2 that the detection is likely due to the ISW effect and not contamination or systematics). Instead, we display in Fig. 7 the signed-intensity values on the sky for the scale ($\theta_{\rm hw} \simeq 400'$) corresponding to the most significance detection of correlation. Due to the strength of the correlation, it is possible to see it by eye between the WMAP (Fig. 7 (a)) and NVSS data (Fig. 7 (c)). We consider only the signed-intensity of local features here since this morphological measure corresponds to the most significant detection of correlation made in these local morphological analyses.

4.2 Foregrounds and systematics

To test whether the correlation detected in the preceding subsection is perhaps due to foreground contamination or instrumental systematics in the WMAP data, we examine the correlation signals computed using individual WMAP bands and difference maps in place of the WMAP co-added map. Again, we consider only the signed-intensity of local features here since this morphological measure corresponds to the most significant detection of correlation made in these local morphological analyses. In Fig. 8 (a) we plot the morphological signed-intensity correlation of the NVSS data with each of the individual WMAP band maps (constructed from the mean signal observed by all receivers in that band), while in Fig. 8 (b) we plot the correlation for maps constructed from band differences (constructed from differences of signals observed by various receivers).

Any correlation induced by unremoved foreground contamination in the WMAP data is expected to exhibit a frequency dependence, reflecting the emission law of the foreground component. However, the same correlation signal is observed in each of the WMAP bands and no frequency dependence is apparent (see Fig. 8 (a)). Furthermore, the difference map W−V−Q is clearly contaminated by foreground contributions, while having a minimal CMB contribution. No correlation is detected in this difference map (see Fig. 8 (b)). Consequently, we may conclude that foreground contamination is not the source of the correlation detected.

The same correlation signal is observed in each WMAP band (see Fig. 8 (a)). Furthermore, this signal is not present in any of the difference maps constructed for each given band (see Fig. 8 (b)), which contain no CMB or foreground contributions. These findings suggest that the correlation detected is not due to systematics in the WMAP data.

The preliminary tests performed in this subsection indicate that it is unlikely that either foregrounds or systematics are responsible for the correlation detected in the signed-intensity of local features. This strongly suggests that the ISW effect is responsible for the statistically significant correlation detected in this section between the WMAP and NVSS data.

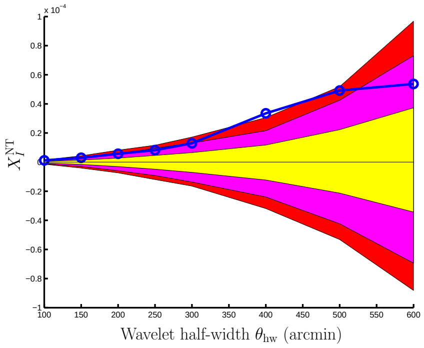

(a) Signed-intensity

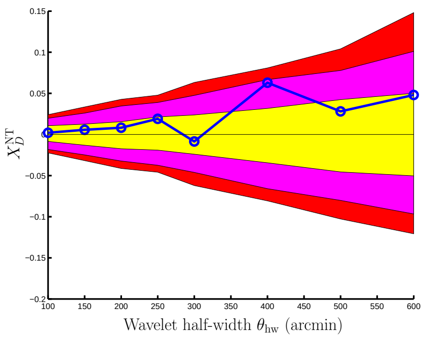

(b) Orientation

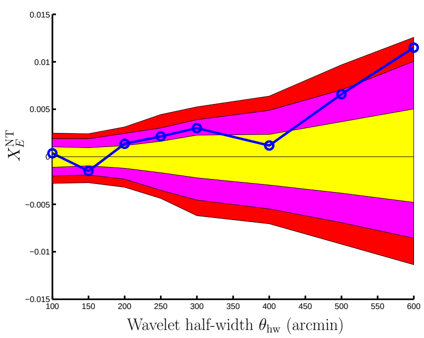

(c) Elongation

Figure 6. Correlation statistics computed for each morphological measure in the local morphological analysis, from the WMAP co-added map and the NVSS map. Significance levels obtained from the 1000 Monte Carlo simulations are shown by the shaded regions for 68% (yellow/light-grey), 95% (magenta/grey) and 99% (red/dark-grey) levels. The different ranges of the correlations for the signed-intensity, orientation, and elongation are consistent with our rough estimations of the standard deviations for each local morphological measure in each of the two data sets (see section 3.2).

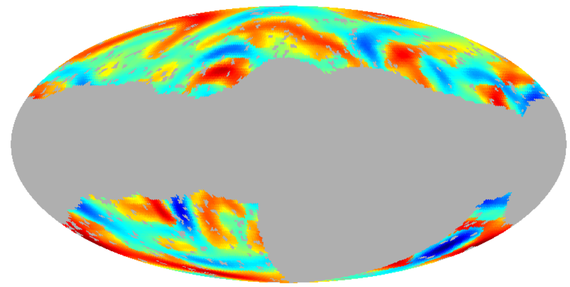

(a) WMAP for independent features

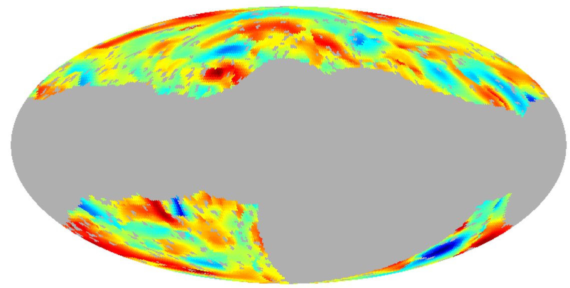

(b) WMAP for features matched to NVSS orientations

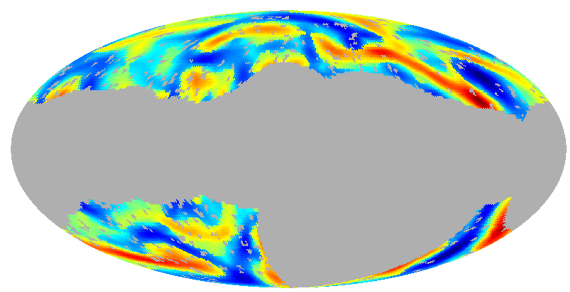

(c) NVSS

Figure 7. Morphological signed-intensity maps (Mollweide projection) corresponding to the scale ($\theta_{\rm hw} \simeq 400'$) on which the maximum detections of correlation are made. In panel (a) signed-intensities are shown for local features extracted independently from the WMAP co-added data, whereas in panel (b) signed-intensities are shown for local features in the WMAP co-added data that are matched in orientation to local features in the NVSS data. Due to the strength of the correlation in the data, it is possible to observe the correlation both between maps (a) and (c) and between maps (b) and (c) by eye.

5 MATCHED INTENSITY CORRELATION

In this section we present the results obtained from the matched intensity analysis described in section 3.4 to examine the WMAP and NVSS data for possible correlation. In this setting the orientation of local features extracted from the WMAP data at each position on the sky are matched to orientations extracted from the NVSS data. It therefore no longer makes sense to correlate the orientation or elongation of features between the two data sets. Correlations are detected between the signed-intensity of matched features and are examined to determine whether they are due to foreground contamination or instrumental systematics, or whether they are indeed induced by the ISW effect.

5.1 Detections

The correlation statistics computed from the WMAP and NVSS data for the signed-intensity of matched features are displayed in Fig. 9. Significance levels computed from the Monte Carlo simulations are again shown on each plot. A non-zero correlation signal is clearly present. A strong detection at 99.2% significance is made in the correlation of signed-intensities of local features for wavelet half-width $\theta_{\rm hw} \simeq 400'$. This correlation deviates from the mean of the Monte Carlo simulation by 2.6 standard deviations. Note that these significance measures are again based on an *a posteriori* scale selection.

We also compute the *a priori* significance of the detection of correlation when considering all scales in aggregate, taking into account the correlation between scales. This is based on the χ^2 test described in section 4.1. For this case we detect a highly significant correlation at a level of 99.9%.

Although it is possible to localise regions on the sky that con-

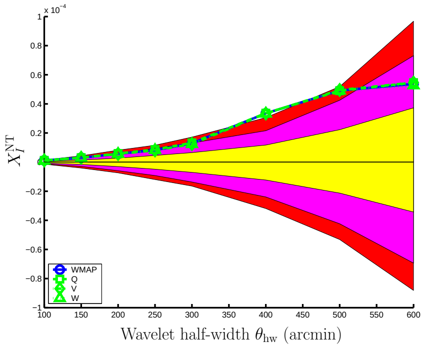

(a) Individual band maps

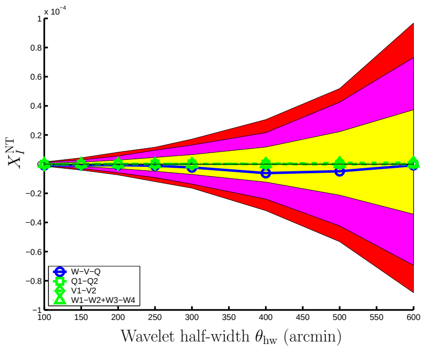

(b) Difference maps

Figure 8. Correlation statistics computed for the signed-intensity of features in the local morphological analysis, from the WMAP individual band and difference maps and the NVSS map. Significance levels obtained from the 1000 Monte Carlo simulations are shown by the shaded regions for 68% (yellow/light-grey), 95% (magenta/grey) and 99% (red/dark-grey) levels.

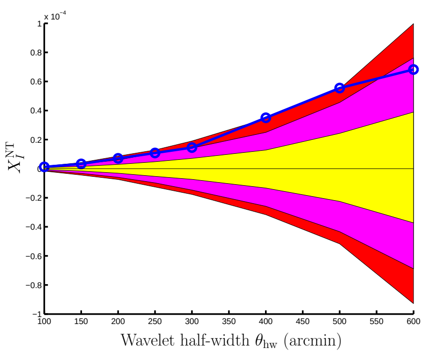

Figure 9. Correlation statistics computed for signed-intensity in the matched intensity analysis, from the WMAP co-added map and the NVSS map. Significance levels obtained from the 1000 Monte Carlo simulations are shown by the shaded regions for 68% (yellow/light-grey), 95% (magenta/grey) and 99% (red/dark-grey) levels.

tribute most significantly to the correlation detected, we again do not do this since the ISW signal is expected to be weakly distributed over the entire sky (as described in section 4.1). Instead, we display in Fig. 7 the signed-intensity of matched features on the sky for the scale ($\theta_{\mathrm{hw}} \simeq 400'$) corresponding to the most significance detection of correlation using this analysis. Due to the strength of the correlation, it is again possible to see it by eye between the WMAP (Fig. 7 (b)) and NVSS data (Fig. 7 (c)).

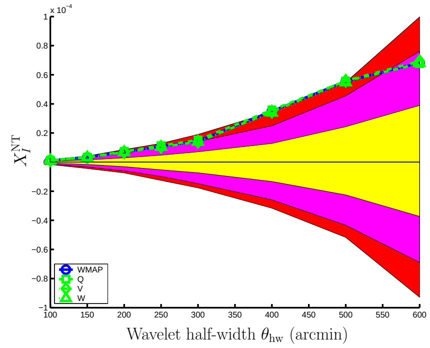

(a) Individual band maps

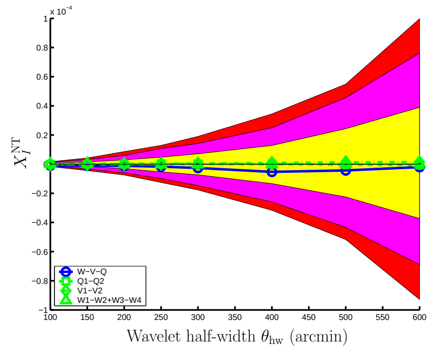

(b) Difference maps

Figure 10. Correlation statistics computed for the signed-intensity in the matched intensity analysis, from the WMAP individual band and difference maps and the NVSS map. Significance levels obtained from the 1000 Monte Carlo simulations are shown by the shaded regions for 68% (yellow/light-grey), 95% (magenta/grey) and 99% (red/dark-grey) levels.

5.2 Foregrounds and systematics

For this analysis procedure we also check whether the correlation detected is perhaps due to foreground contamination or systematics. We follow the same procedure outlined in section 4.2. The correlation signals computed for the matched intensity analysis using individual WMAP bands and differences maps in place of the WMAP co-added data are plotted in Fig. 10. No frequency dependence is observed between the signals computed for the individual band maps (see Fig. 10 (a)), neither is any correlation observed in the foreground contaminated W−V−Q map (see Fig. 10 (b)). These findings suggest that foreground contributions are not responsible for the correlation detected in this analysis. Furthermore, the same correlation signal is observed in each individual band (see Fig. 10 (a)), but is not present in any of the difference maps for each given band (see Fig. 10 (b)). This indicates that systematics are not responsible for the correlation detected in this analysis. These results again strongly suggest that the ISW effect is responsible for the correlation detected between the WMAP and NVSS data in this second analysis based on the signed-intensity of matched features.

6 CONCLUSIONS

We have presented the first direct analysis of local morphological measures on the sphere defined through a steerable wavelet analysis. Using the wavelet on the sphere constructed from the second derivative of a Gaussian, we are able to define three quantities to characterise the morphology of local features: the signed-intensity, orientation and elongation. These local morphological measures provide additional probes to search for correlation between the CMB and LSS of the Universe that may have been induced by the ISW effect.

Based on the morphological measures defined, we perform two distinct analyses to search for correlation between the WMAP and NVSS data. The first procedure, the local morphological analysis, correlates the morphological measures of local features extracted independently in the two data sets. This provides the most general analysis and does not make any assumption regarding possible correlation in the data. The second procedure, the matched intensity analysis, is based on the assumption that local features of the LSS are somehow included in the local features of the CMB. Local features are extracted from the WMAP data that are matched in orientation to features in the NVSS data and the signed-intensities of these features are correlated between the two data sets. Although the two analysis procedures performed are obviously different conceptually, we have shown that they differ practically also. Regardless of the procedure adopted, in the absence of an ISW effect the WMAP and NVSS data should be independent and no correlation should be present in any of the local morphological measures considered. However, strong detections are obtained in the correlation of the signed-intensities of local features using both analysis procedures. The most significant detection is made in the matched intensity analysis at 99.9% significance, when all scales are considered in aggregate. Moreover, in the local morphological analysis, moderate detections are also made in the correlation of the orientation and elongation of local features. In both analyses foreground contamination and instrumental systematics have been ruled out as the source of the correlation observed. This strongly suggests that the correlation detected is indeed due to the ISW effect. Since the ISW effect only exists in a universe with dark energy or a non-flat universe, and strong constraints have been placed on the flatness of the Universe (Spergel et al. 2007), the detection of the ISW effect made here can be inferred as direct and independent evidence for dark energy.

In previous wavelet analyses to detect the ISW effect, theoretical predictions are derived for the wavelet correlation in order to constrain dark energy parameters of cosmological models (Vielva et al. 2006; McEwen et al. 2007b; Pietrobon et al. 2006). As already discussed, our detections give a new insight on the nature of the correlation between the CMB and the LSS, in terms of the signed-intensity, orientation and elongation of local features. This might in turn help to better understand the nature of dark energy through new constraints on dark energy parameters. However, our steerable wavelet analysis is complicated by allowing the orientation of wavelet coefficients to vary as a function of the data. The derivation of the theoretical correlation for each local morphological measure is not easily tractable. We are currently exploring this issue in more detail and leave any attempts to constrain standard dark energy parameters to a future work. We also intend to explore the use of this, and other wavelet-based, ISW detections to investigate perturbations in the dark energy fluid and to constrain the sound speed of dark energy (see *e.g.* Weller & Lewis 2003; Bean & Doré 2004).

ACKNOWLEDGEMENTS

We thank Patricio Vielva and Enrique Martínez-González for providing the preprocessed NVSS data. JDM is supported by PPARC. YW acknowledges support of the Swiss National Science Foundation (SNF) under contract No. 200021-107478/1. He is also postdoctoral researcher of the Belgian National Science Foundation (FNRS). Some of the results in this paper have been derived using the `HEALPix` package (Górski et al. 2005). We acknowledge the use of the Legacy Archive for Microwave Background Data Analysis (LAMBDA). Support for LAMBDA is provided by the NASA Office of Space Science.

REFERENCES

Afshordi N., 2004, Phys. Rev. D., D70, 083536, astro-ph/0401166
Afshordi N., Loh Y.S., Strauss M.A., 2004, Phys. Rev. D., D69, 083524, astro-ph/0308260
Allen S.W., Schmidt R.W., Fabian A.C., 2002, Mon. Not. Roy. Astron. Soc., 334, L11, astro-ph/0205007
Antoine J.P., Vandergheynst P., 1998, J. Math. Phys., 39, 8, 3987
Barreiro R.B., Martínez-González E., Sanz J.L., 2001, Mon. Not. Roy. Astron. Soc., 322, 411, astro-ph/0009365
Barreiro R.B., Sanz J.L., Martínez-González E., Cayon L., Silk J., 1997, Astrophys. J., 478, 1, astro-ph/9612114
Bean R., Doré O., 2004, Phys. Rev. D., 69, 083503, astro-ph/0307100
Bennett C.L., et al., 2003a, Astrophys. J. Supp., 148, 97, astro-ph/0302208
Bennett C.L., et al., 2003b, Astrophys. J. Supp., 148, 1, astro-ph/0302207
Boldt E., 1987, Phys. Rep., 146, 215
Boughn S., Crittenden R., 2004, Nature, 427, 45, astro-ph/0305001
Boughn S., Crittenden R., 2005, Mon. Not. Roy. Astron. Soc., 360, 1013, astro-ph/0408242
Boughn S.P., Crittenden R.G., 2002, Phys. Rev. Lett., 88, 021302, astro-ph/0111281
Cabré A., Fosalba P., Gaztañaga E., Manera M., 2007, Mon. Not. Roy. Astron. Soc., 381, 1347, astro-ph/0701393
Cabré A., Gaztañaga E., Manera M., Fosalba P., Castander F., 2006, Mon. Not. Roy. Astron. Soc., 372, L23, astro-ph/0603690
Condon J.J., Cotton W.D., Greisen E.W., Yin Q.F., Perley R.A., Taylor G.B., Broderick J.J., 1998, Astrophys. J., 115, 1693
Corasaniti P.S., Giannantonio T., Melchiorri A., 2005, Phys. Rev. D., D71, 123521, astro-ph/0504115
Crittenden R.G., Turok N., 1996, Phys. Rev. Lett., 76, 575, astro-ph/9510072
Fosalba P., Gaztañaga E., 2004, Mon. Not. Roy. Astron. Soc., 350, L37, astro-ph/0305468
Fosalba P., Gaztañaga E., Castander F., 2003, Astrophys. J., 597, L89, astro-ph/0307249
Gaztañaga E., Manera M., Multamäki T., 2006, Mon. Not. Roy. Astron. Soc., 365, 171, astro-ph/0407022
Giannantonio T., et al., 2006, Phys. Rev. D., 74, 6, 063520, astro-ph/0607572
Górski K.M., Hivon E., Banday A.J., Wandelt B.D., Hansen F.K., Reinecke M., Bartelmann M., 2005, Astrophys. J., 622, 759, astro-ph/0409513
Gurzadyan V.G., et al., 2005, Mod. Phys. Lett. A, 20, 813, astro-ph/0503103
Hinshaw G., et al., 2007, Astrophys. J. Supp., 170, 288, astro-ph/0603451

Hu W., Scranton R., 2004, Phys. Rev. D., D70, 123002, astro-ph/0408456
Jarrett T.H., Chester T., Cutri R., Schneider S., Skrutskie M., Huchra J.P., 2000, Astron. J., 119, 2498, astro-ph/0004318
Komatsu E., et al., 2003, Astrophys. J. Supp., 148, 119, astro-ph/0302223
LoVerde M., Hui L., Gaztanaga E., 2007, Phys. Rev. D., 75, 043519, astro-ph/0611539
Maddox S.J., Efstathiou G., Sutherland W.J., Loveday J., 1990, Mon. Not. Roy. Astron. Soc., 242, 43
McEwen J.D., Hobson M.P., Mortlock D.J., Lasenby A.N., 2007a, IEEE Trans. Sig. Proc., 55, 2, 520, astro-ph/0506308
McEwen J.D., Vielva P., Hobson M.P., Martínez-González E., Lasenby A.N., 2007b, Mon. Not. Roy. Astron. Soc., 373, 1211, astro-ph/0602398
Monteserín C., Barreiro R.B., Sanz J.L., Martínez-González E., 2005, Mon. Not. Roy. Astron. Soc., 360, 9, astro-ph/0511308
Nolta M.R., et al., 2004, Astrophys. J., 608, 10, astro-ph/0305097
Padmanabhan N., Hirata C.M., Seljak U., Schlegel D.J., Brinkmann J., Schneider D.P., 2005, Phys. Rev. D., D72, 043525, astro-ph/0410360
Perlmutter S., et al., 1999, Astrophys. J., 517, 565, astro-ph/9812133
Pietrobon D., Balbi A., Marinucci D., 2006, Phys. Rev. D., 74, 4, 043524, astro-ph/0606475
Planck collaboration, 2005, ESA Planck blue book, Technical Report ESA-SCI(2005)1, ESA, astro-ph/0604069
Pogosian L., 2005, JCAP, 0504, 015, astro-ph/0409059
Pogosian L., 2006, New Astron. Rev., 50, 932, astro-ph/0606626
Pogosian L., Corasaniti P.S., Stephan-Otto C., Crittenden R., Nichol R., 2005, Phys. Rev. D., D72, 103519, astro-ph/0506396
Rassat A., Land K., Lahav O., Abdalla F.B., 2006, ArXiv, astro-ph/0610911
Riess A.G., et al., 1998, Astron. J., 116, 1009, astro-ph/9805201
Sachs R.K., Wolfe A.M., 1967, Astrophys. J., 147, 73
Scranton R., et al., 2003, ArXiv, astro-ph/0307335
Spergel D.N., et al., 2007, Astrophys. J. Supp., 170, 377, astro-ph/0603449
Vielva P., Martínez-González E., Tucci M., 2006, Mon. Not. Roy. Astron. Soc., 365, 891, astro-ph/0408252
Weller J., Lewis A.M., 2003, Mon. Not. Roy. Astron. Soc., 346, 987, astro-ph/0307104
Wiaux Y., Jacques L., Vandergheynst P., 2005, Astrophys. J., 632, 15, astro-ph/0502486
Wiaux Y., Jacques L., Vielva P., Vandergheynst P., 2006, Astrophys. J., 652, 820, astro-ph/0508516
Wiaux Y., McEwen J.D., Vielva P., invited contribution, 2007, J. Fourier Anal. and Appl., 13, 4, 477, arXiv:0704.3144
York D. G. *et al.* (SDSS collaboration), 2000, Astron. J., 120, 1579, astro-ph/0006396